

Search for continuous gravitational waves from neutron stars in five globular clusters in the first part of the fourth LIGO–Virgo–KAGRA observing run

DAMON H. T. CHEUNG ¹, KEITH RILES ¹, RAFEL AMENGUAL ², PREET BAXI,¹ ALICIA CALAFAT ²,
ANAMARIA EFFLER ³, TABATA AIRA FERREIRA ⁴, EVAN GOETZ ⁵, DAVID KEITEL ², TOM KIMPSON ^{6,7},
ALAN M. KNEE ¹, JOAN-RENÉ MÉROU ², QUYNH LAN NGUYEN ⁸, JOSEPH O’LEARY ^{6,7}, ORNELLA J. PICCINNI ²,
ALICIA M. SINTES ² AND KARL WETTE ⁹

¹*Department of Physics, University of Michigan, 450 Church St, Ann Arbor, MI 48109*

²*Departament de Física, Universitat de les Illes Balears, IAC3–IEEC, Carretera de Valldemossa, km 7.5, 07122 Palma, Spain*

³*LIGO Livingston Observatory, Livingston, LA 70754, USA*

⁴*Instituto Nacional de Pesquisas Espaciais, 12227-010 São José dos Campos, São Paulo, Brazil*

⁵*Department of Physics & Astronomy, University of British Columbia, Vancouver, BC V6T 1Z1, Canada*

⁶*School of Physics, University of Melbourne, Parkville, VIC 3010, Australia*

⁷*Australian Research Council Centre of Excellence for Gravitational Wave Discovery (OzGrav), Parkville, VIC 3010, Australia*

⁸*Phenikaa University, Nguyen Trac Street, Duong Noi, Hanoi, Vietnam*

⁹*OzGrav-ANU, Centre for Gravitational Astrophysics, Australian National University, Canberra ACT 2601, Australia*

(Dated: March 6, 2026)

ABSTRACT

We present the results of directed searches for continuous gravitational waves from unknown neutron stars in five Milky Way globular clusters. We carry out the searches in the LIGO data from the first eight months of the fourth LIGO–Virgo–KAGRA observing run using the WEAVE semi-coherent program, which sums matched-filter detection-statistic values over many time segments spanning the observation period. No gravitational wave signal is detected in the search band of 20–475 Hz for assumed source ages greater than 300 years. Injections of simulated continuous wave signals in the data indicate that we achieve the most sensitive results to date across most of the explored parameter space volume, obtaining median 95% confidence level upper limits as low as $\sim 4.2 \times 10^{-26}$ near 282 Hz for NGC 6397.

Keywords: Keywords

1. INTRODUCTION

Continuous gravitational waves (CWs) are faint, long-duration, quasi-monochromatic signals that remain undetected despite extensive searches (for recent reviews of searches, see Tenorio et al. 2021; Piccinni 2022; Riles 2023; Wette 2023). Rapidly rotating, non-axisymmetric neutron stars (NSs) in the Milky Way are promising sources of CWs (for reviews of emission mechanisms, see Lasky 2015; Glampedakis & Gualtieri 2018). Young NSs are particularly attractive targets because they have had less time to anneal structural deformations. Furthermore, many known young pulsars exhibit high spin-down magnitudes, which are compatible with a de-

tectable contribution from gravitational-wave (GW) energy loss (Aharonian et al. 2005).

On the other hand, millisecond pulsars (MSPs) with high spin frequencies, thought to form via “recycling” of a NS’s rotation by accretion from a binary companion, have much lower spin-down magnitudes, consistent with low asymmetry (Lorimer 2008). Yet MSPs are attractive targets precisely because their high spins means that a low asymmetry can still produce detectable radiation. In the following, we use “MSP” as a shorthand for a fast-spinning ($f_{\text{rot}} \gtrsim 100$ Hz) NS, whether or not the star emits pulsations and whether or not emitted pulses are beamed toward the Earth.

With these considerations in mind, we target NSs in globular clusters (GCs). The high stellar density in GC cores increases the likelihood of encounters with debris disks (Wang et al. 2006) or planets (Bailes et al. 2011;

Wolszczan & Frail 1992; Spiewak et al. 2018; Behrens et al. 2020; Nițu et al. 2022), triggering bombardment episodes. This scenario could lead to an old, annealed isolated NS acquiring a new non-axisymmetry and hence the high spin-down rate characteristic of young stars. Another possibility is that successive close encounters lead to MSP formation in a newly formed accreting binary system, followed by binary disruption, leaving an isolated MSP (Dunn et al. 2025).

In this work, we analyze the first eight months (O4a) of LIGO (Aasi et al. 2015a; Abbott et al. 2016; Abac et al. 2025; Capote et al. 2025) data from the fourth LIGO-Virgo-KAGRA observing run to search for CW signals from unknown NSs in the central regions of the Terzan 10, NGC104, NGC 6397, NGC 6544, and NGC 6540 GCs. Using a template-based semi-coherent search based on the \mathcal{F} -statistic (Jaranowski et al. 1998a), we probe a wide range of spin-down parameters, but find no evidence of an astrophysical signal. Hence, upper limits on strain amplitude and astrophysical constraints on fiducial ellipticity ϵ_0 and r-mode amplitude α_0 are set.

Our analysis achieves improved sensitivity compared to previous searches for NGC 6544 (Abbott et al. 2017) and the recent results for NGC 6397, NGC 6544, and NGC 6540 (Dunn et al. 2025). We report the most stringent strain upper limits to date for these targets while covering a broader spin-down range. Furthermore, we present the first directed searches for Terzan 10 and NGC 104. Our upper limits beat the age-based limit on GW strain amplitude across all frequencies > 100 Hz for sources younger than 50 kyr. This limit is the indirect upper bound obtained by assuming that all rotational energy lost since birth is emitted as GWs.

The remainder of this article is organized as follows: Section 2 details the data set used. Section 3 outlines the selection criteria for the GCs in this search. Section 4 describes the signal model used. Section 5 briefly describes the \mathcal{F} -statistic, the semi-coherent search method, and the WEAVE infrastructure. Section 6 outlines the search strategy, including follow-up analysis using WEAVE. Section 7 presents the results of the search, including the astrophysical constraints. Finally, Section 8 concludes with a discussion of the results and prospects for future searches.

2. DATASET

We analyze data from the LIGO Livingston (L1) and LIGO Hanford (H1) detectors (Aasi et al. 2015b) collected during the first eight months of the fourth Advanced LIGO and Virgo observing run (O4a). It began May 24, 2023 (15:00:00 UTC) and ended January 16,

2024 (16:00:00 UTC) (Abac et al. 2025). Data were used only when the detectors were in science observing mode (Goetz & Riles 2025), corresponding to duty factors of 69.0% for L1 and 67.5% for H1. Figure 1 illustrates the timeline of the data collected from both detectors over this period. The Virgo detector (Acernese et al. 2015) was not included in this analysis as it joined the O4 run later, on April 10, 2024, while the KAGRA detector (Akutsu et al. 2020) is scheduled to join by the end of the observing run. For a detailed description of the upgrades to the Advanced LIGO, Advanced Virgo, and KAGRA detectors in preparation for O4, we refer the reader to Appendix A of Abac et al. (2024).

Detector sensitivity improved significantly across all frequencies in this observing run compared to O3, particularly above 400 Hz (Capote et al. 2025; Jia et al. 2024; Ganapathy et al. 2023; Wade et al. 2025). The LIGO detectors are calibrated using photon radiation pressure actuation, in which an amplitude-modulated laser beam is directed onto the end test masses to induce a known change in arm length (Goetz et al. 2009; Karki et al. 2016; Viets et al. 2018). The maximum systematic error in strain amplitude and phase calibration is estimated to be within 10% and 10 degrees (68% confidence interval), respectively, for both detectors over the entire frequency band analyzed in this search (Dartez et al. 2025).

Prior to the search, the dataset underwent cleaning procedures to assess data quality and mitigate the effects of instrumental artifacts (Soni et al. 2025). As in previous Advanced LIGO observing runs (Covas et al. 2018), instrumental “lines” (sharp peaks in fine-resolution, run-averaged H1 and L1 spectra) are marked, and where possible, their instrumental or environmental sources are identified (Goetz et al. 2024; Goetz & Riles 2025). The resulting database of artifacts was used to veto spurious signal candidates arising from the search; however, no frequency bands were vetoed *a priori*. Consistent with the O3 run, the number of instrumental lines identified in H1 data for O4a is significantly larger than in L1.

Another class of artifacts observed in both detectors consists of frequent, loud “glitches” (short, high-amplitude instrumental transients), with the majority of their spectral power concentrated below ~ 500 Hz (Abbott et al. 2021a). To mitigate their impact on CW searches, a glitch-gating algorithm was applied (Davis et al. 2024) to excise these transients. For this analysis, we use the G02 version of gated 30-minute Short Fourier Transforms (SFTs) (Allen et al. 2025).

3. TARGETS

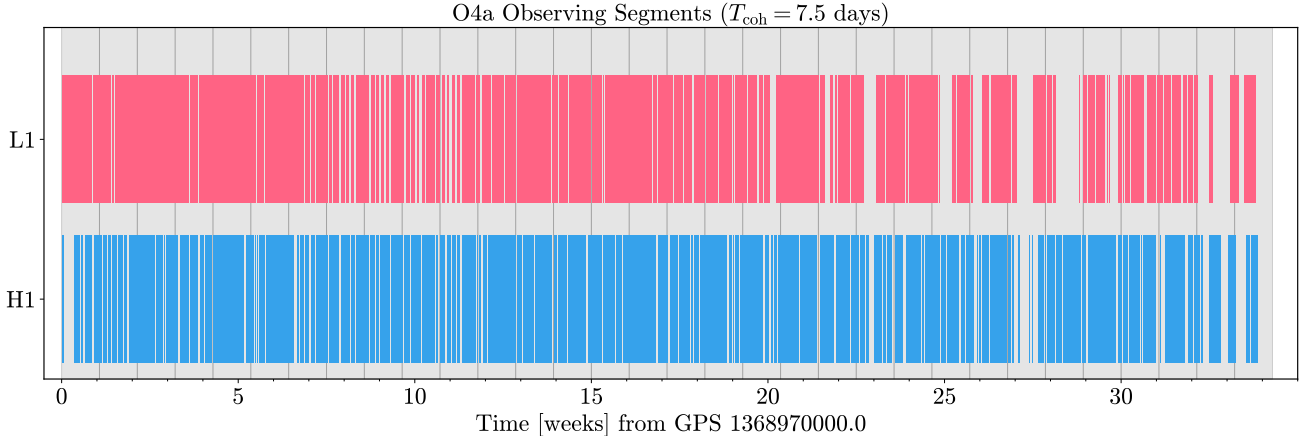


Figure 1. Data collected from the H1 and L1 detectors during the first eight months of the fourth observing run (O4a), spanning from May 24, 2023 (15:00:00 UTC) to January 16, 2024 (16:00:00 UTC). The shaded segments represent the 7.5-day coherence segments used in the initial stage of the search (detailed in Section 5).

In the frequency band where current ground-based detectors are most sensitive, the canonical sources of CWs are rapidly rotating, non-axisymmetric NSs in the Milky Way. GCs are promising environments for such sources because of their dense stellar cores and high rates of dynamical interactions. These environments frequently give birth to low-mass X-ray binaries (LMXBs) (Katz 1975; Clark 1975; Pooley et al. 2003), which are progenitors of MSPs via accretion (Alpar et al. 1982). Additionally, close encounters in dense cluster cores can destabilize debris disks or planetary orbits around NSs, triggering bombardment episodes that funnel material into magnetic field-aligned “mountains” that emit CWs. In this paper, we implicitly consider both scenarios: we seek “young” (post-disruption) stars at low frequencies and moderately fast-spinning MSPs that exist as isolated NSs following the disruption of a recycled binary system by a secondary encounter (Dunn et al. 2025).

Because of limited computational resources, we cannot search for CW signals from all known GCs. Therefore, we employ specific figures of merit to rank clusters based on their likelihood of hosting detectable CW sources. First, we consider the age-based upper limit on CW strain amplitude for a compact object. This limit is derived by assuming that the star’s current rotation frequency is significantly lower than its birth frequency and that its spin-down history has been dominated by GW energy loss (Wette et al. 2008):

$$h_{\text{age}} = [2.3 \times 10^{-24}] \left[\frac{1 \text{ kpc}}{d} \right] \left[\frac{1000 \text{ yr}}{\tau} \right]^{1/2} \left[\frac{I_{zz}}{I_0} \right]^{1/2}, \quad (1)$$

where τ is the source age, d is the distance, and I_{zz} denotes the principal moment of inertia about the rotation axis, with a fiducial value $I_0 = 10^{38} \text{ kg} \cdot \text{m}^2$. To apply

this relation to a cluster population, we use an effective age that scales inversely with the encounter rate, representing the mean time since the last bombardment. This yields a figure of merit proportional to the number of potentially GW-emitting “young” NSs (Abbott et al. 2017):

$$\Gamma^{1/2} d^{-1} = \rho_c^{3/4} r_c d^{-1}, \quad (2)$$

where Γ represents the encounter rate, ρ_c is the core density, and r_c is the core radius.

We also consider the figure of merit introduced by Dunn et al. (2025), which accounts for the probability of binary disruption by replacing the age with the inverse of the binary encounter rate:

$$\gamma^{1/2} d^{-1} = \rho_c^{1/4} r_c^{-1/2} d^{-1}, \quad (3)$$

where γ denotes the binary encounter rate. This metric is inversely proportional to the square root of a binary’s lifetime before disruption by a secondary encounter. Consequently, a higher value implies a larger expected population of isolated MSPs. We ranked the GCs from the Harris catalog (Harris 1996) using both Eq. 2 and Eq. 3.

The top three GCs based on Eq. 2 are Terzan 10, NGC 6544, and NGC 104. Based on Eq. 3, the top three candidates are NGC 6397, NGC 6544, and NGC 6540. Since NGC 6544 appears in the top tier for both metrics, we select a total of five GCs as targets for this search. Detailed properties of these targets, including sky locations, core radii, central luminosity densities, tidal radii, and distances, are provided in Table 1.

Figure 2 displays the central density versus core radius for Milky Way GCs, with data points colored according to the number of known pulsars (with $2f_{\text{rot}} \in$

	α (Right Ascension)	δ (Declination)	r_c [arcmin]	$\log_{10}(\rho_c/L_\odot\text{pc}^{-3})$	r_t (arcmin)	d [kpc]
Terzan 10	18 ^h 03 ^m 36.4 ^s	−26°04′21″	0.90′	4.64	1.91′	5.8
NGC 104 (47 Tuc)	00 ^h 24 ^m 05.67 ^s	−72°04′52.6″	0.36′	4.88	2.85′	4.5
NGC 6397	17 ^h 40 ^m 42.09 ^s	−53°40′27.6″	0.05′	5.76	0.61′	2.3
NGC 6544	18 ^h 07 ^m 20.58 ^s	−24°59′50.4″	0.05′	6.06	0.26′	3.0
NGC 6540	18 ^h 06 ^m 08.60 ^s	−27°45′55.0″	0.03′	5.85	0.37′	5.3

Table 1. Sky locations (Right Ascension α and Declination δ), core radius r_c , central luminosity density ρ_c , tidal radius r_t , and distance d for each targeted globular cluster from the Harris catalog (Harris 1996).

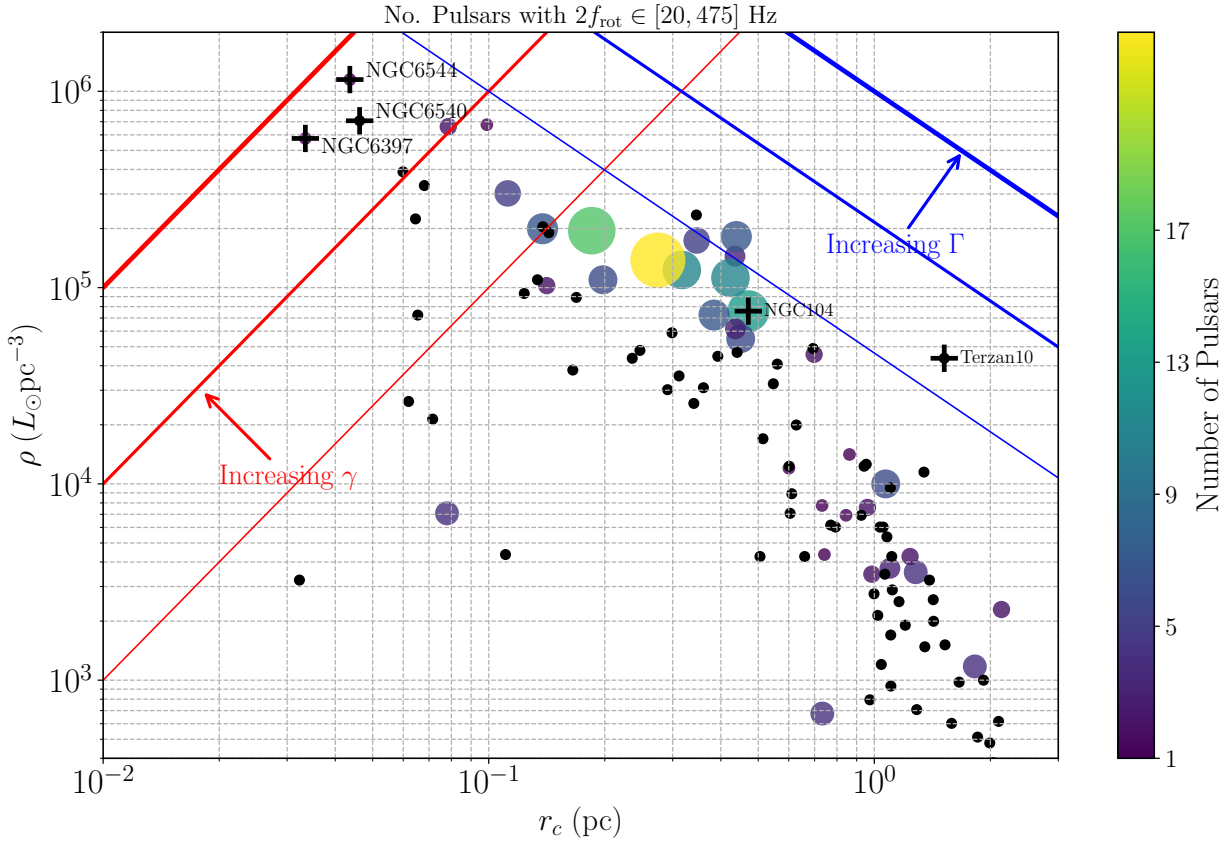


Figure 2. Central density as a function of core radius for Milky Way globular clusters from Harris (1996). The color of each point indicates the number of pulsars observed in that cluster. Blue lines indicate lines of constant formation rate Γ (Eq. 2), and red lines indicate constant binary encounter rate γ (Eq. 3). The targets selected for this search are marked with black crosses. The figures of merit (Eqs. 2-3) used to prioritize target selection also consider the distance d to each cluster, not shown in this diagram.

[20, 475] Hz) discovered in each cluster. The blue contours represent lines of constant stellar encounter rate Γ , while the red contours indicate lines of constant binary encounter rate γ . Clusters with large known pulsar populations generally lie in the upper-right region where Γ is high, consistent with the success of Γ in predicting pulsar abundance (Verbunt & Freire 2014). Conversely,

clusters with comparably high binary encounter rates γ do not currently show rich pulsar populations. This discrepancy may stem from observational biases or the simplifying assumptions inherent in the binary encounter rate model. Nevertheless, we target top candidates from both figures of merit to ensure comprehensive coverage in our search.

4. SIGNAL MODEL

We consider a rapidly rotating, non-axisymmetric neutron star with a time-varying quadrupole moment. This source emits circularly polarized gravitational radiation along the rotation axis, linearly polarized radiation in directions perpendicular to the rotation axis, and elliptically polarized radiation in the general case. The strain signal $h(t)$ measured by the detector is given by:

$$h(t) = h_0 \left[F_+(t, \alpha, \delta, \psi) \frac{1 + \cos^2 \iota}{2} \cos \Phi(t) + F_\times(t, \alpha, \delta, \psi) \cos \iota \sin \Phi(t) \right], \quad (4)$$

where h_0 is the intrinsic strain amplitude and $\Phi(t)$ is the signal phase. The functions F_+ and F_\times characterize the detector’s response to “+” and “ \times ” polarizations, respectively (Abbott et al. 2008), determined by the source sky location (right ascension α , declination δ) and the polarization angle ψ . The inclination angle ι describes the orientation of the star’s rotation axis relative to the line of sight. The linear polarization case ($\iota = \pi/2$) is the most unfavorable, with the GW flux impinging on the detectors possessing eight times less incident strain power than for circularly polarized waves ($\iota = 0, \pi$) with the same intrinsic strain amplitude h_0 .

The phase evolution of the signal is described in the Solar System Barycenter (SSB) reference frame. We approximate the phase using a Taylor expansion in time:

$$\Phi(t) = \phi_0 + 2\pi \sum_{k=0}^s \frac{f^{(k)}(t_0)}{(k+1)!} (t - t_0)^{k+1}, \quad (5)$$

where $f^{(k)}$ denotes the k -th time derivative of the frequency at the reference time t_0 (taken as the midpoint of O4a: GPS 1379338000). In this work, we search up to the second order ($s = 2$) of frequency derivatives: frequency f , spin-down \dot{f} , and the second derivative \ddot{f} . When expressed as a function of the local time of ground-based detectors, Eq. 5 acquires sky-position-dependent Doppler shift terms due to the relative motion between the source and the detector, as well as the relativistic Einstein and Shapiro time delays.

The relationship between the gravitational-wave frequency f and the stellar rotation frequency f_{rot} depends on the specific emission mechanism. For example, mass quadrupoles emit at $f = 2f_{\text{rot}}$ (Ushomirsky et al. 2000; Cutler 2002; Lasky & Melatos 2013), while r-modes emit at $f \approx 4f_{\text{rot}}/3$ (Andersson 1998; Owen et al. 1998; Idrisy et al. 2015; Caride et al. 2019; Gittins & Andersson 2023).

4.1. Parameter Space

We search a GW frequency band from 20 to 475 Hz. The lower bound is dictated by the rapid deterioration of detector sensitivity due to seismic noise below 20 Hz. The upper bound is chosen to avoid the forests of “violin modes” near 500 Hz (and near integer multiples thereof). These frequencies correspond to vibration resonances of the 16 suspension fibers supporting the four primary mirrors in each interferometer. While less severe resonances from suspension fibers supporting the beam splitter mirrors contaminate narrow bands between 300 and 400 Hz, the region between 475 Hz and the lowest violin mode harmonic (just below 500 Hz) is particularly problematic due to non-linear couplings that create frequency “shoulders” and sidebands around the violin modes. Consequently, we set a ceiling of 475 Hz. This range is astrophysically and computationally motivated: it targets the expected frequencies of young isolated neutron stars and the lower-frequency population of MSPs, while significantly reducing the computational cost associated with expanding the parameter space volume.

The search range for frequency derivatives is governed by the assumed minimum age τ of the source. Following previous directed CW searches (Abadie et al. 2010; Aasi et al. 2015c; Abbott et al. 2019, 2021b, 2022; Wang & Riles 2024), we define the bounds by assuming a power-law spin-down model, $\dot{f} \propto -f^n$, where the braking index n ranges between 2 and 7. This covers multiple spin-down mechanisms, including magnetic dipole emission ($n = 3$), GW quadrupole emission (gravitar scenario Palomba 2005, $n = 5$), and r-mode emission ($n = 7$). Adopting the conservative approach from Abbott et al. (2022) and Wang & Riles (2024), we extend the upper limit on \dot{f} to zero to account for time-dependent braking indices:

$$-\frac{\dot{f}}{\tau} \leq \dot{f} \leq 0, \quad \frac{2\dot{f}^2}{f} \leq \ddot{f} \leq \frac{7\dot{f}^2}{f}. \quad (6)$$

This strategy of searching “with eyes wide open” increases robustness against model uncertainties. Table 2 lists the maximum absolute values of \dot{f} and \ddot{f} searched.

\dot{f} range (Hz/s) @20 Hz	$[-2.1 \times 10^{-9}, 0]$
\ddot{f} range (Hz/s ²) @20 Hz	$[0, 1.6 \times 10^{-18}]$
\dot{f} range (Hz/s) @200 Hz	$[-2.1 \times 10^{-8}, 0]$
\ddot{f} range (Hz/s ²) @200 Hz	$[0, 1.5 \times 10^{-17}]$
\dot{f} range (Hz/s) @475 Hz	$[-5.0 \times 10^{-8}, 0]$
\ddot{f} range (Hz/s ²) @475 Hz	$[0, 3.7 \times 10^{-17}]$

Table 2. The search ranges for \dot{f} and \ddot{f} at 20, 200, and 475 Hz.

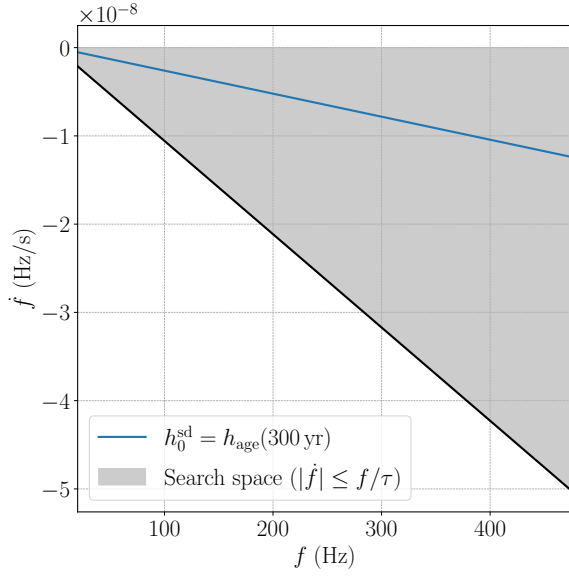


Figure 3. Comparison of search range and the required spin-down rate \dot{f}_{age} (Eq. 8, blue) to exceed the age-based strain limit, assuming a source with an age of 300 years. The black solid line indicates the maximum spin-down covered in this search. The search range fully encompasses the physically motivated region.

To validate the sensitivity of our search configuration, we consider the age-based strain limit. This is the strain amplitude h_0^{sd} derived by assuming that the star’s entire spin-down energy budget is converted into GWs:

$$h_0^{\text{sd}} = [2.6 \times 10^{-25}] \left[\frac{1 \text{ kpc}}{d} \right] \left[\frac{I_{zz}}{I_0} \right]^{1/2} \left[\frac{100 \text{ Hz}}{f} \right]^{1/2} \times \left[\frac{|\dot{f}|}{10^{-11} \text{ Hz/s}} \right]^{1/2}. \quad (7)$$

By equating the age-based limit (Eq. 1) with the spin-down limit (Eq. 7), we determine the minimum spin-down rate $|\dot{f}|_{\text{age}}$ required for a source of age τ to produce a detectable signal:

$$|\dot{f}_{\text{age}}| = [7.8 \times 10^{-10} \text{ Hz/s}] \left[\frac{1000 \text{ yr}}{\tau} \right] \left[\frac{f}{100 \text{ Hz}} \right]. \quad (8)$$

Figure 3 illustrates our search space (shaded region), which extends up to the characteristic spin-down $\dot{f} = -f/\tau$. We compare this region to the \dot{f}_{age} curve (blue) required to surpass the age-based limit for a source with an age of 300 years. The comparison confirms that our search range is sufficiently broad to detect signals surpassing the age-based limit for a 300-year-old source across the entire frequency band. Furthermore, at the maximum spin-down rate covered by our search, we beat the age-based limit for sources as young as ~ 80 years.

5. METHOD

This search relies upon a semi-coherent averaging of the \mathcal{F} -statistic (Jaranowski et al. 1998a; Cutler & Schutz 2005) computed over segments spanning the observation period using the WEAVE infrastructure (Wette et al. 2018). Here, we provide a brief summary of the detection statistic and search method used; we refer the interested reader to the cited references for full details.

5.1. Detection Statistic

The search for CW signals buried in detector noise is formulated as a maximum likelihood detection problem. We assume the detector data $x(t)$ consists of a signal $h(t)$ additive to zero-mean Gaussian noise $n(t)$:

$$x(t) = n(t) + h(t). \quad (9)$$

The log-likelihood ratio $\ln \Lambda$ deciding between the signal hypothesis and the noise hypothesis is given by:

$$\ln \Lambda = (x|h) - \frac{1}{2}(h|h). \quad (10)$$

Here, $(a|b)$ denotes the standard noise-weighted inner product (scalar product), defined as:

$$(a|b) = 4\text{Re} \int_0^\infty \frac{\tilde{a}(f)\tilde{b}^*(f)}{S_n(f)} df, \quad (11)$$

where $\tilde{a}(f)$ is the Fourier transform of $a(t)$, where “*” denotes complex conjugation, and where $S_n(f)$ is the one-sided power spectral density of the detector noise.

Maximizing this likelihood over the full parameter space is computationally prohibitive for long observation periods. However, the signal $h(t)$ depends linearly on four amplitude parameters \mathcal{A}^μ (functions of $h_0, \cos \iota, \psi, \phi_0$). Following Jaranowski et al. (1998a), we decompose the signal into a linear combination of four basis functions $h_\mu(t)$:

$$h(t) = \sum_{\mu=1}^4 \mathcal{A}^\mu h_\mu(t), \quad (12)$$

where the basis functions $h_\mu(t)$ depend only on the phase evolution parameters $\vec{\lambda} = (\alpha, \delta, f, \dot{f}, \dots)$ and detector geometry. Substituting this decomposition into the log-likelihood ratio allows us to rewrite it in vector notation:

$$\ln \Lambda = \vec{\mathcal{A}} \cdot \vec{x} - \frac{1}{2} \vec{\mathcal{A}} \cdot \mathcal{M} \cdot \vec{\mathcal{A}}. \quad (13)$$

Here, \vec{x} represents the projections of the data onto the basis functions, and \mathcal{M} is the antenna pattern matrix:

$$x_\mu = (x|h_\mu), \quad (14)$$

$$\mathcal{M}_{\mu\nu} = (h_\mu|h_\nu). \quad (15)$$

To analytically marginalize over the unknown amplitude parameters, we find the estimators $\vec{\mathcal{A}}_{\text{ML}}$ that maximize the likelihood by solving $\partial(\ln \Lambda)/\partial \mathcal{A}^\mu = 0$. This yields $\mathcal{A}_{\text{ML}}^\mu = (\mathcal{M}^{-1})^{\mu\nu} x_\nu$. Substituting these estimators back into the likelihood equation yields the \mathcal{F} -statistic:

$$2\mathcal{F} = 2 \ln \Lambda(\vec{\mathcal{A}}_{\text{ML}}) = \vec{x} \cdot \mathcal{M}^{-1} \cdot \vec{x}. \quad (16)$$

Using $2\mathcal{F}$ as the detection statistic significantly reduces the computational burden by eliminating the need to search explicitly over h_0 , ι , ψ , and ϕ_0 .

In Gaussian noise with no signal present, $2\mathcal{F}$ follows a central χ^2 distribution with 4 degrees of freedom. In the presence of a signal, it follows a non-central χ^2 distribution with a non-centrality parameter $\rho^2 \propto h_0^2 T_{\text{coh}}/S_n(f)$. This parameter encapsulates the signal strength relative to the noise, scaled by the coherence time T_{coh} and modified by the source orientation and detector response.

5.2. Semi-coherent Search

Despite the efficiency of the analytical maximization, a fully coherent search over the entire observing run T_{obs} remains computationally intractable because the density of templates required to cover the parameter space scales with a high power of the observation time. To address this, we employ a semi-coherent approach. We partition the total observation time T_{obs} into N_{seg} segments of duration T_{coh} and compute $2\mathcal{F}$ coherently for each segment. We then sum these values incoherently across segments while maintaining consistency in the frequency evolution. Rather than a simple sum at fixed parameter-space points, this process involves mapping templates from a finely spaced semi-coherent grid to the nearest templates in coarser, segment-specific grids (as detailed in Section 5.3).

The semi-coherent detection statistic, denoted $2\hat{\mathcal{F}}$, is defined as the mean of the $2\mathcal{F}$ -statistic values over the N_{seg} segments:

$$2\hat{\mathcal{F}} = \frac{1}{N_{\text{seg}}} \sum_{i=1}^{N_{\text{seg}}} 2\mathcal{F}_i. \quad (17)$$

In the absence of a signal, the quantity $N_{\text{seg}} 2\hat{\mathcal{F}}$ follows a χ^2 distribution with $4N_{\text{seg}}$ degrees of freedom. Consequently, $2\hat{\mathcal{F}}$ has an expected value of 4 and a standard deviation of $\sqrt{8/N_{\text{seg}}}$. The presence of a signal induces an offset in the mean proportional to the non-centrality parameter averaged over the segments.

5.3. The WEAVE Infrastructure

To use the detection statistic to search for CW signals over a range of parameter space, a template bank is required. The WEAVE software infrastructure provides

a systematic approach to covering the parameter space volume in a templated search to ensure acceptable loss of signal-to-noise ratio (SNR) for true signals lying between template points (Wette et al. 2018). The WEAVE program combines recent developments in template placement to use an optimal parameter-space metric (Wette & Prix 2013; Wette 2015) and optimal template lattices (Wette 2014).

In brief, a template grid in the parameter space is created for each time segment—a grid suitable for computing the $2\mathcal{F}$ for a coherence time $T_{\text{coh}} = T_{\text{obs}}/N_{\text{seg}}$. The spacing of the grid points for the phase evolution parameters $\Delta\vec{\lambda}$ is determined by the maximum mismatch parameter:

$$m_{\text{coh}} = 1 - \frac{\rho(\vec{\mathcal{A}}, \vec{\lambda}^s + \Delta\vec{\lambda})}{\rho(\vec{\mathcal{A}}, \vec{\lambda}^s)} = g_{ij}(\vec{\mathcal{A}}, \vec{\lambda}^s) \Delta\lambda_i \Delta\lambda_j, \quad (18)$$

where g_{ij} is the metric of the template bank, and $\vec{\lambda}^s$ represents the true phase evolution parameters of the signal. It represents the maximum fractional loss in SNR due to a true signal not coinciding with a search template.

Separately, a much finer grid is defined for the full observation period with respect to the reference time t_0 . This grid uses a semi-coherent mismatch parameter m_{semi} , analogous to m_{coh} , but defined as the average of the coherent mismatch values over all segments. The choice of m_{semi} is an empirical trade-off between sensitivity and computational cost. During initialization, the WEAVE package creates a mapping between each point in the fine semi-coherent template grid and the nearest corresponding point in each of the coarser segment grids, accounting for frequency evolution. The semi-coherent detection statistic $2\hat{\mathcal{F}}$ is then constructed for each semi-coherent template using this mapping.

6. SEARCH CONFIGURATION

In this section, we describe how to set up and conduct the search, as well as how to follow up candidates for signal validation using the WEAVE program.

6.1. Initial stage

We adopt the same mismatch parameters, m_{coh} and m_{semi} , as used in Abbott et al. (2021b) for WEAVE. The initial search stage uses a coherence time of $T_{\text{coh}} = 7.5$ days and a single sky-location template targeting the center of the cluster (see Table 1). While a grid of sky templates would be required to maintain uniform sensitivity across the entire parameter space, we restricted the initial search to a single central template due to computational costs. Consequently, the sensitivity to signals originating farther from the search direction degrades as the frequency increases.

Search jobs are carried out in 0.1-Hz bands of f , with further divisions in \dot{f} , \ddot{f} to keep each job’s computational duration less than 24 hours, for practical reasons. Table 3 summarizes the configuration parameters of the search and the width of \dot{f} , \ddot{f} sub-ranges for each search job.

Coherent mismatch m_{coh}	0.1
Semi-coherent mismatch m_{semi}	0.2
Coherence time T_{coh}	7.5 days
Number of segments N_{seg}	32
\dot{f} width	2×10^{-9} Hz/s
\ddot{f} width	5×10^{-18} Hz/s ²

Table 3. WEAVE configuration parameters, coherence time, and the width of \dot{f} , \ddot{f} sub-ranges for each search job used in the initial searches.

Each individual job returns the (f, \dot{f}, \ddot{f}) values of the 1000 templates (“top-list”) with the largest (“loudest”) $2\hat{\mathcal{F}}$ values.

To select the candidates from the initial search result, we sum up the number of templates for each 1-Hz band and calculate the nominal threshold

$$2\hat{\mathcal{F}}_{\text{thresh}} = \frac{1}{N_{\text{seg}}} \cdot \text{CDF}_{\chi^2}^{-1} \left(1 - \frac{1}{N_{\text{temp}}}, 4N_{\text{seg}} \right), \quad (19)$$

where $\text{CDF}_{\chi^2}^{-1}$ is the inverse cumulative distribution function (CDF) of the χ^2 distribution with $4N_{\text{seg}}$ degrees of freedom, evaluated at $1 - 1/N_{\text{temp}}$ percentile, and N_{temp} is the number of templates in a 1-Hz band. This threshold is set based on a signal-free χ^2 distribution such that the expected number of candidates is one per 1-Hz band, assuming Gaussian noise (In practice, non-Gaussian artifacts lead to much higher outlier counts). Templates with $2\hat{\mathcal{F}}$ values exceeding this threshold are considered candidates. In some cases, strong instrumental lines can lead to more than 1000 templates from a single job that exceed the threshold. We refer to those cases as “saturated” since potentially interesting templates may be suppressed by the top-list cap.

6.2. Follow-up stage

For non-saturated jobs, outliers exceeding the threshold $2\hat{\mathcal{F}}_{\text{thresh}}(f)$ are followed up in a sequential procedure. The outliers are first clustered by grouping those within $\pm 3\Delta f^{(n)}$, where $\Delta f^{(n)}$ represents the average template spacing for the n -th frequency derivative. We retain only the loudest outlier in each cluster as the seed for the next stage. In each subsequent follow-up step, the coherence time T_{coh} is doubled (and hence the number of segments

N_{seg} is halved). Higher-order terms in the phase model $\Phi(t)$ are included to better capture the signal, based on the coherence time and frequency-derivative order configured for each stage (see Table 4). Because the non-centrality parameter for the $2\hat{\mathcal{F}}$ detection statistic scales approximately linearly with T_{coh} , one expects a nominal doubling of the $2\hat{\mathcal{F}}$ value.

To determine the expected increase in the $2\hat{\mathcal{F}}$ for true signals, we perform 50 software injections per 1-Hz band. Signals are injected with random frequency parameters and sky positions drawn from the target’s central region. Each injection uses a strain amplitude equal to the upper limit $h_0^{95\%}$ corresponding to 95% detection efficiency (see Sec. 7.2). For NGC 6397, NGC 6544, and NGC 6540, we draw positions within the tidal radius (r_t). However, for Terzan 10 and NGC 104, the tidal radii are too large to be covered effectively by the single-template strategy employed in the initial search stage; therefore, we restrict the injections to the core radius (r_c) for these two targets, so that the derived criteria are sufficient to capture signals originating from the relevant region.

Using these injections, we determine the threshold $2\hat{\mathcal{F}}$ values required to recover the signals. The resulting required ratio increase in $2\hat{\mathcal{F}}$ to recover injected signals above the threshold is listed in Table 5.

For targets other than Terzan 10, we use a single sky point (fixed at the cluster center) for both the initial search and all subsequent follow-up stages. As the coherence time increases in the follow-up stages, the template grid becomes finer, and signals originating farther from the center experience a greater fractional loss in $2\hat{\mathcal{F}}$ due to mismatch. We account for this by adjusting our detection criteria rather than adding more sky points. The required $2\hat{\mathcal{F}}$ increase threshold is empirically determined via software injections: signals are injected with random source positions within the radius we aim to cover but are recovered using only the single central sky search template. Consequently, the injection analysis yields lower, less stringent thresholds for targets with larger radii to maintain the targeted signal recovery efficiency. For example, as shown in Table 5, we consider an NGC 6397 outlier with a ratio increase above 57% in the 4th stage to be a surviving candidate. This threshold is lower than the 62% required for NGC 6540 and NGC 104, and the 65% for NGC 6544, consistent with their respective radii (where NGC 6397 > NGC 6540 \sim NGC 104 > NGC 6544).

For Terzan 10, the initial search is performed using the single central sky template, just as with the other targets. This single template is capable of detecting candidates from the wider region, albeit with reduced efficiency for off-center sources. However, be-

cause Terzan 10 has the largest angular radius we aim to cover, continuing to use a single sky template for follow-up would result in such severe signal loss that a true signal's $2\hat{\mathcal{F}}$ increase would be indistinguishable from a noise-induced outlier. Therefore, for every Terzan 10 outlier above the initial $2\hat{\mathcal{F}}_{\text{thresh}}(f)$ threshold, we generate nine follow-up jobs for the first stage instead of one. These copies cover the same frequency search range but use distinct sky positions: one fixed at the cluster center and eight surrounding points positioned roughly at the midpoint between the center and the edge of the target area. This 9-point grid ensures that at least one template is close enough to an off-center source to effectively recover it. We calculate the required detection ratio using the loudest $2\hat{\mathcal{F}}$ from these nine jobs relative to the initial seed. The search sky position is then fixed to the position of this loudest job for all subsequent follow-up stages. This strategy allows us to significantly reduce the offset between the source position and the search direction at an early stage, before the coherence time becomes too long.

At later follow-up stages, we retain only the top 10 loudest survivors for each seed from previous stage. Thus, while all outliers above the $2\hat{\mathcal{F}}_{\text{thresh}}(f)$ threshold are evaluated in the initial search stage, only the top 10 loudest survivors are followed up in successive stages until the coherence time T_{coh} reaches 120 days. We have confirmed that these threshold criteria achieve over 95% recovery efficiency for the injected signals, with source right ascension and declination randomly drawn within the tidal/core radius region of the GCs.

The loudest outlier in each saturated sub-range is followed up using the same procedure. This ensures that an unusually strong signal causing the saturation is not discarded due to the top-list cap.

	T_{coh}	highest order in $\Phi(t)$
Initial search	7.5 days	2
1st follow-up	15	2
2nd follow-up	30	2
3rd follow-up	60	3
4th follow-up	120	4

Table 4. Coherence time and frequency derivative order configuration for different stages.

7. RESULTS

7.1. Candidates

	1st follow-up	2nd	3rd	4th
Terzan 10	46%	43%	62%	55%
NGC 104	35%	41%	60%	62%
NGC 6397	35%	42%	58%	57%
NGC 6544	35%	42%	60%	65%
NGC 6540	34%	41%	58%	62%

Table 5. $2\hat{\mathcal{F}}$ increase requirement for each globular cluster across follow-up stages for the five targets.

We searched for the GCs Terzan 10, NGC 6544, NGC 104, NGC 6397, and NGC 6540 using O4a data. The initial search yielded approximately 3.4 , 5.2 , 5.3 , 3.2 , and 3.7×10^5 outliers above the $2\hat{\mathcal{F}}$ threshold, respectively, in bands not excluded by severe instrumental artifacts. These outliers were then subjected to the clustering and hierarchical follow-up procedure described in Sec. 6.2. The number of clustered outliers at each stage is presented in Table 6. Parameters of the surviving outliers after the last follow-up stage are listed in Appendix. A

	Follow-up stages				
	Stage 0	1st	2nd	3rd	4th
Terzan 10	1.8×10^5	3.0×10^3	362	28	0
NGC 104	2.3×10^5	1.2×10^4	2,922	231	18
NGC 6397	2.6×10^5	9,864	2,644	1,492	72
NGC 6544	1.7×10^5	5,697	1,301	119	10
NGC 6540	1.9×10^5	6,970	1,509	1,106	87

Table 6. Number of outlier clusters for each target surviving after each stage.

To assess the credibility of these remaining outliers at $T_{\text{coh}} = 120$ days as coming from an astrophysical source or from instrumental contamination, we construct spectrograms using O4a data overlain with strong simulated signals with the same frequency parameters as the loudest outlier in each cluster. We plot the spectrogram using the cumulative averaged power, which is then summed daily across all 1800-second SFTs within each day of the O4a observation period. Figure 4 shows an example narrowband H1 spectrogram used to veto the loudest outlier in the 283 Hz band for NGC 6397.

In Figure 4, a prominent instrumental line artifact (bright horizontal band) is visible near 283.9 Hz, overlapping with the simulated signal (dark colors) during approximately the last 60-day segment of the O4a observation period, a period when the signal template's

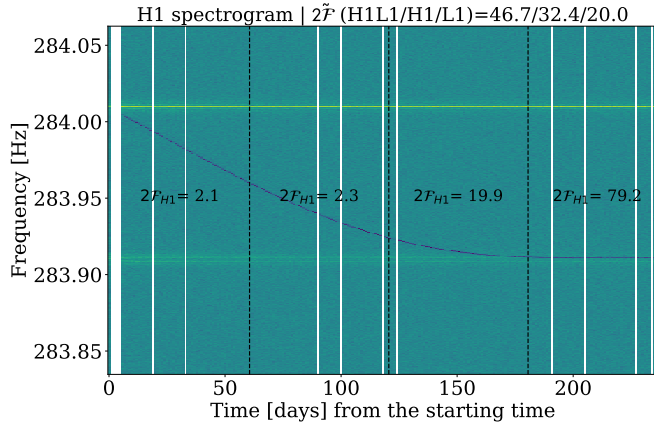


Figure 4. H1 spectrogram near 283.9 Hz (bright) with injected signal using the NGC 6397 outlier’s parameters (dark). The spectrogram is generated by taking the daily sum of the cumulative averaged power across all 1800-second SFTs within each day. In the last 60-day segment, the simulated signal overlaps with an instrumental line artifact, causing it to appear as an outlier at the $T_{\text{coh}} = 120$ days follow-up stage.

Doppler modulation is nearly stationary. The simulated signal is based on the loudest real outlier’s parameters, which has $2\hat{\mathcal{F}} = 46.7$ at $T_{\text{coh}} = 120$ days, with single detector statistics of $2\hat{\mathcal{F}}_{\text{H1}} = 32.4$ and $2\hat{\mathcal{F}}_{\text{L1}} = 20.0$. The $2\mathcal{F}_{\text{H1}}$ value for the four 60-day segments, also displayed in the spectrogram, reveals a significant bias toward the final segment, confirming that the $2\hat{\mathcal{F}}$ is predominantly influenced by the instrumental line artifact during that period. Hence, we do not consider it to be a credible astrophysical signal.

After applying the spectrogram-based line veto to all outliers surviving the 4th stage of follow-up, no candidates remained for any of the five targets. We conclude that there is no significant evidence in this analysis for a CW signal from the compact objects at the central region of the targeted GCs.

7.2. Upper limits

Given the absence of a detection, we determine 95%-efficiency upper limits on strain amplitude $h_0^{95\%}$ for each 1-Hz band, excluding saturated 0.1-Hz sub-bands.

To obtain $h_0^{95\%}$, we conduct software injections of signals with varying amplitudes, drawing frequencies uniformly within each 1-Hz band (excluding saturated bands). The parameters $\cos \iota$, ψ , \dot{f} , and \ddot{f} are also drawn uniformly, while the sky locations (α, δ) are drawn isotropically from the center region of the GC within the tidal/core radius. An injection is deemed detectable if its $2\hat{\mathcal{F}} \geq 2\hat{\mathcal{F}}_{\text{thresh}}(f)$ with the initial search setup (assuming all outliers above this threshold have been fol-

lowed up and excluded). This procedure is repeated for different signal amplitudes h_0 , and the detection fraction is fitted using a sigmoid function:

$$p(h_0) = \frac{1}{1 + \exp\left(\frac{a-h_0}{b}\right)}, \quad (20)$$

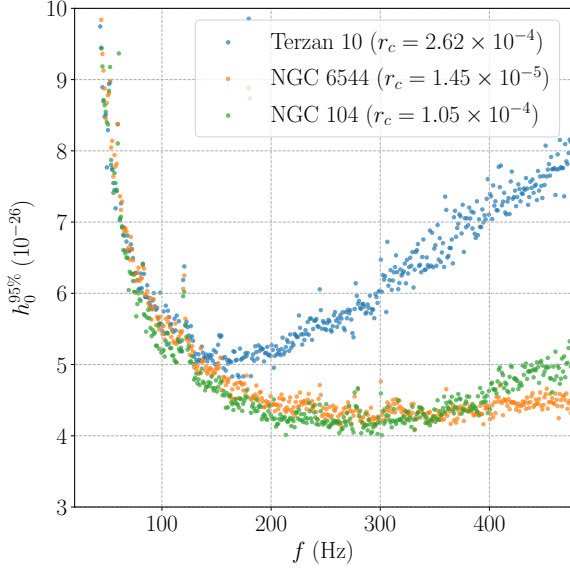
where $p(h_0)$ represents the fraction of detected injections for a given h_0 , and a and b are the parameters of the sigmoid function. The number of injections is chosen to ensure that the statistical uncertainty in the estimated $h_0^{95\%}$ is below 5%.

Figure 5 presents the 95% confidence level upper limits on the GW strain amplitude h_0 as a function of frequency. Panel (a) displays the results for Terzan 10, NGC 6544, and NGC 104, assuming signals originate from the central region defined by the core radius, r_c . Panel (b) illustrates the upper limits for NGC 6397, NGC 6544, and NGC 6540, assuming a source distribution extending out to the tidal radius, r_t . Note that the upper limits derived for Terzan 10 degrade more significantly at high frequencies. This degradation arises because the signal population is distributed over a larger sky area, while we use a single sky template fixed at the cluster center for the initial search stage. The components of the metric associated with sky position scale with the square of the frequency ($g_{\alpha\alpha}, g_{\delta\delta} \propto f^2$). Consequently, the mismatch due to spatial offsets is more severe at higher frequencies, causing the effective coverage of a single template to shrink. Since we limited the initial search stage to a single sky template, signals originating further from the search direction suffer increasingly severe SNR loss. Thus, the elevated upper limit reflects the larger spatial spread of the source population, rather than a loss of sensitivity for signals originated near the search center.

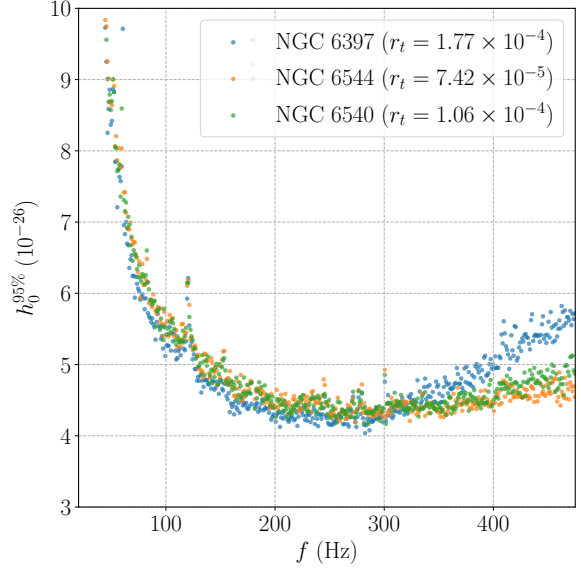
We compare our upper limits to the sensitivity from Dunn et al. (2025), as shown in Figure 6. To facilitate a direct comparison with previous searches using O3 data, we calculate the effective upper limits. The effective strain amplitude $h_{0,\text{eff}}$ is defined as

$$(h_{0,\text{eff}})^2 = h_0^2 \frac{[(1 + \cos^2 \iota)/2]^2 + \cos^2 \iota}{2}. \quad (21)$$

Similar to the procedure described above for $h_0^{95\%}$, we determine the 95% effective upper limits ($h_{0,\text{eff}}^{95\%}$) directly through software injections. However, we vary $h_{0,\text{eff}}$ values rather than h_0 . For each simulated signal at a given $h_{0,\text{eff}}$, we draw the inclination angle uniformly in $\cos \iota$ and invert Eq. 21 to calculate the corresponding intrinsic strain h_0 required for the injection. All other injection parameters are drawn as previously described. We then fit the detection fraction and estimate the 95% effective



(a) Terzan 10, NGC 6544, and NGC 104



(b) NGC 6397, NGC 6544, and NGC 6540

Figure 5. Gravitational wave strain amplitude upper limits (95% efficiency) in each 1-Hz band. (a) Results for Terzan 10, NGC 6544, and NGC 104 assuming signals originate from a central region with radius equal to the core radius r_c . (b) Results for NGC 6397, NGC 6544, and NGC 6540 assuming signals originate from within the tidal radius r_t . The degradation of the upper limit at higher frequencies is more pronounced for searches covering the larger radius.

upper limits, ensuring the statistical uncertainty in the estimated $h_{0,\text{eff}}^{95\%}$ is below 5%. Our results improve upon those from [Dunn et al. \(2025\)](#) across 100–475 Hz. Notably, we achieve stricter effective upper limits of ~ 1.7 – 2.3×10^{-26} , improving upon their limits by ~ 30 – 40% . Furthermore, our search explores a spin-down range 1–2 orders of magnitude broader than the parameter space considered in their work.

To quantify the sensitivity of a search pipeline, independent of the data quality, a figure of merit known as the sensitivity depth \mathcal{D} ([Behnke et al. 2015](#)) is commonly used:

$$\mathcal{D}(f) \equiv \frac{\sqrt{\bar{S}_h(f)}}{h_0^{95\%}}, \quad (22)$$

where $\sqrt{\bar{S}_h(f)}$ is an estimate of the effective strain amplitude spectral noise density. For non-stationary detector noise, we use an inverse-noise weighted estimate for each frequency bin j from the two interferometers:

$$\bar{S}_h(f_j) = \frac{\sum_i w_{ij} S_h(f_i)}{\sum_i w_{ij}}, \quad (23)$$

where i ranges over Fourier transforms of 30-minute segments of the H1 and L1 data, and w_{ij} is a weight equal to the average inverse power spectral density for 50 neighboring frequency bins $j' \neq j$ in the same Fourier transform i :

$$w_{ij} \equiv \frac{1}{50} \sum_{j'} \frac{1}{S_h(f_{j'})} \quad (24)$$

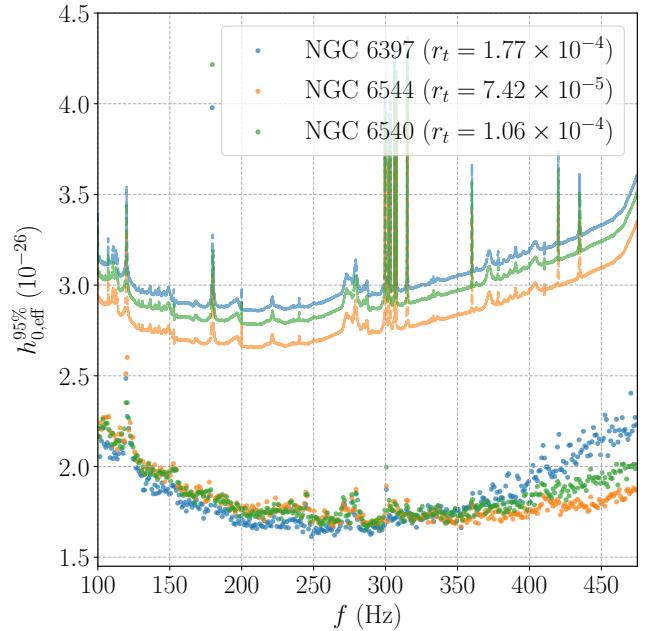


Figure 6. Effective gravitational wave strain amplitude upper limits (95% efficiency) in each 1-Hz band for NGC 6397 (blue), NGC 6544 (orange), and NGC 6540 (green). The dashed lines represent the corresponding sensitivity from ([Dunn et al. 2025](#)), with the spin-down range restricted to $|f| \leq 5 \times 10^{-10}$ Hz/s.

for $|j' - j| \leq 25$ and $j' \neq j$. This weighting de-emphasizes noisy segments of data, similarly to the weighting used to define the \mathcal{F} -statistic.

Table 7 shows the resulting sensitivity depths at 200 Hz for the five targets, as well as the averaged sensitivity depth where frequencies below 50 Hz have been excluded from consideration because the combination of highly disturbed bands and substantial mismatch between H1 and L1 strain noise levels would lead to artificially inflated sensitivity depth values.

	$\mathcal{D}^{95\%}$ [Hz $^{-1/2}$]	
	200 Hz	Ave.
Terzan 10	70.5	69.8
NGC 104	87.2	89.3
NGC 6397	88.6	86.5
NGC 6544	84.3	87.1
NGC 6540	87.3	86.7

Table 7. Sensitivity depths $\mathcal{D}^{95\%}$ for the targeted globular clusters at 200 Hz and the averaged depth $\mathcal{D}^{95\%}$ over 50–475 Hz.

7.3. Astrophysical constraints

The GW strain upper limits derived in the previous section can be converted into constraints on the physical properties of the NSs. We consider two emission scenarios: a non-axisymmetric deformation of the star (ellipticity) and unstable r -mode oscillations.

First, for a triaxial neutron star, the strain amplitude is directly related to the fiducial ellipticity, ϵ_0 (Jaranowski et al. 1998b). Assuming a canonical moment of inertia with respect to the rotation axis ($I_{zz} = 10^{38}$ kg m 2), our 95% confidence strain limits ($h_0^{95\%}$) constrain ϵ_0 as a function of frequency via:

$$\epsilon_0^{95\%} = [9.46 \times 10^{-5}] \left[\frac{h_0^{95\%}}{10^{-24}} \right] \left[\frac{d}{1 \text{ kpc}} \right] \left[\frac{100 \text{ Hz}}{f} \right]^2. \quad (25)$$

Alternatively, we consider emission via unstable r -modes (Andersson 1998; Bildsten 1998; Friedman & Morsink 1998; Owen et al. 1998; Kojima 1998). In this model, the gravitational wave frequency is $f \approx (4/3)f_{\text{rot}}$, and the signal strength is governed by the dimensionless amplitude α_0 (Owen 2010):

$$h_0 = [3.6 \times 10^{-23}] \left[\frac{\alpha_0}{0.001} \right] \left[\frac{f}{1 \text{ kHz}} \right]^3 \left[\frac{1 \text{ kpc}}{d} \right]. \quad (26)$$

By inverting this relationship and substituting our upper limits $h_0^{95\%}$ for h_0 , we obtain the 95% confidence limits on the r -mode amplitude:

$$\alpha_0^{95\%} \simeq 0.028 \left[\frac{h_0^{95\%}}{10^{-24}} \right] \left[\frac{d}{1 \text{ kpc}} \right] \left[\frac{100 \text{ Hz}}{f} \right]^3. \quad (27)$$

The resulting astrophysical constraints are presented in Figures 7 and 8, calculated using the distance estimates listed in Table 1. Figure 7 displays the limits for the targets searched over the core radius, while Figure 8 shows the corresponding results for the targets searched over the tidal radius. These constraints enter a physically interesting regime. The derived $\epsilon_0^{95\%}$ values are lower than the theoretically predicted maximum ellipticity, which lies in the range of $\sim 10^{-6}$ – 10^{-4} (Haskell et al. 2007; Johnson-McDaniel & Owen 2013). Similarly, our limits on $\alpha_0^{95\%}$ approach one estimated theoretical maximum amplitude of $\sim 10^{-3}$ (Bondarescu et al. 2009).

8. CONCLUSIONS

We have performed the deepest search for CWs from compact stars in the GCs NGC 6397, NGC 6544, and NGC 6540, covering the region within their tidal radii. Additionally, we present the first directed search for Terzan 10 and NGC 104, targeting the central regions within their core radii. The searches resulted in no detections.

Our analysis achieved 95% confidence level upper limits as low as $\sim 5.1/4.2/4.2/4.4/4.4 \times 10^{-26}$ for Terzan 10/NGC 104/NGC 6397/NGC 6544/NGC 6540 at frequencies near 170/301/282/273/301 Hz, respectively. We observe that using a single sky template to cover a larger spatial extent leads to a more pronounced degradation of the upper limits at higher frequencies compared to searches for clusters with smaller characteristic radii.

We have achieved better sensitivities (and ellipticity/ r -mode constraints) for NGC 6544 compared to (Abbott et al. 2017). Furthermore, our results for NGC 6397, NGC 6544, and NGC 6540 improve upon those from Dunn et al. (2025) across the 100–475 Hz band by 30–40%. We also explore a spin-down range 1–2 orders of magnitude broader than the parameter space considered in their work, allowing us to surpass the age-based limit for 300-year-old sources across the entire frequency band.

Our results have begun to constrain the NS ellipticity and r -mode amplitude within a physically interesting regime, reaching values below the theoretical predicted maximums. As the LIGO, Virgo, and KAGRA detectors continue to improve their strain sensitivities in upcoming observing runs, these searches will dig deeper into the astrophysically plausible parameter space, bringing us progressively closer to the first detection of CWs from GCs.

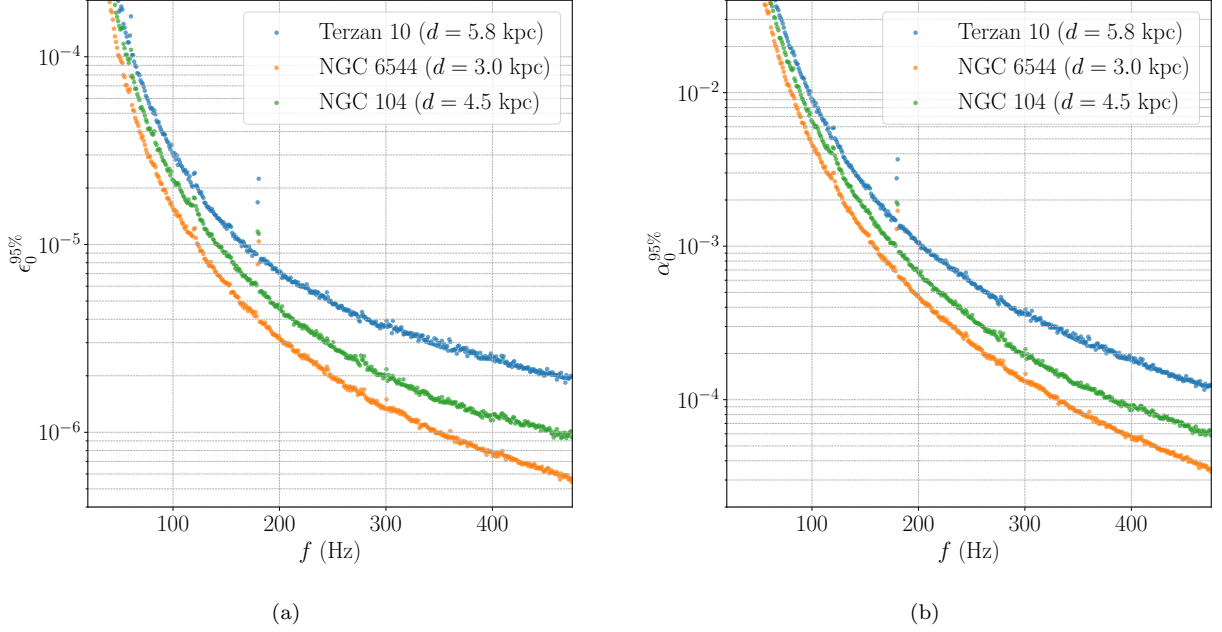


Figure 7. Equatorial ellipticity and r -mode amplitude α_0 upper limits (95% confidence level) in each 1-Hz band for Terzan 10 (blue), NGC 6544 (orange), and NGC 104 (green). These constraints are derived from the strain amplitude upper limits in Figure 5(a) and distances from Table 1.

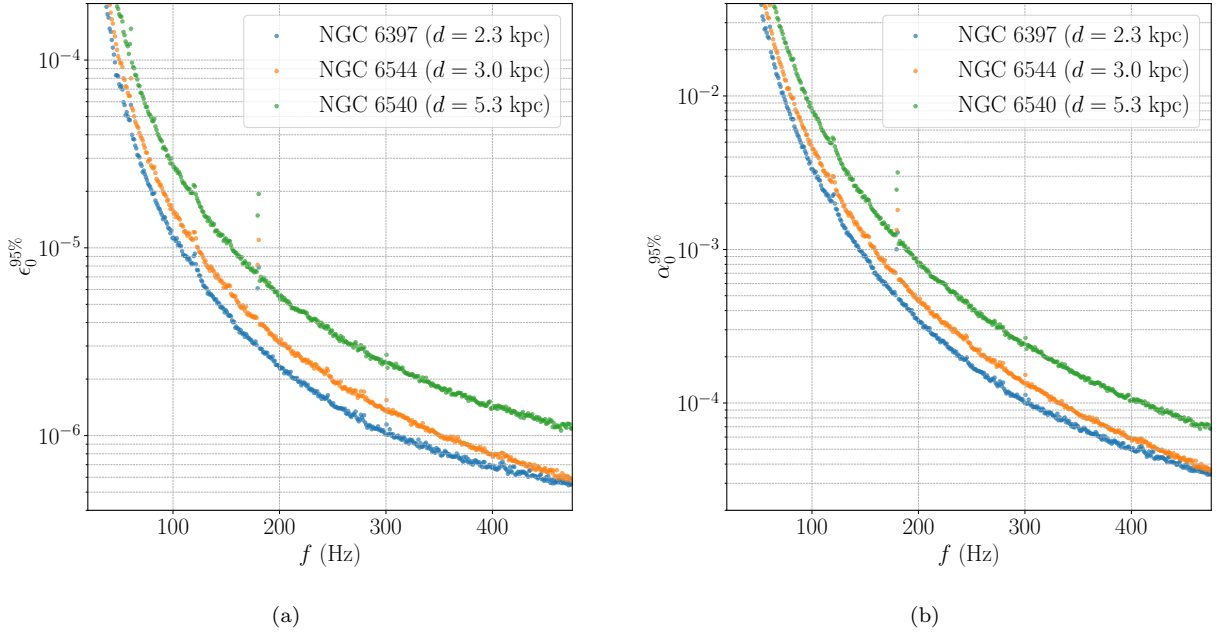


Figure 8. Equatorial ellipticity and r -mode amplitude α_0 upper limits (95% confidence level) in each 1-Hz band for NGC 6397 (blue), NGC 6544 (orange), and NGC 6540 (green). These constraints are derived from the strain amplitude upper limits in Figure 5(b) and distances from Table 1.

9. ACKNOWLEDGMENTS

We gratefully acknowledge useful discussions and long collaboration with current and former colleagues in the LIGO-Virgo-KAGRA continuous waves working group.

We also thank members of the LVK detector characterization group and the spectral line investigations team for valuable identification and mitigation of instrumental artifacts. In addition, we thank Cristiano Palomba

for helpful comments on this manuscript. This work was supported in part by National Science Foundation Awards PHY-2110181 and PHY-2408883.

AC, RJ, DK, JRM, OP and AS were supported by the Universitat de les Illes Balears (UIB) with funds from the Programa de Foment de la Recerca i la Innovació de la UIB 2024-2026 (supported by the yearly plan of the Tourist Stay Tax ITS2023-086); the Spanish Agencia Estatal de Investigación grants PID2022-138626NB-I00, RED2024-153978-E, RED2024-153735-E, funded by MICIU/AEI/10.13039/501100011033 and the ERDF/EU; and the Comunitat Autònoma de les Illes Balears through the Conselleria d'Educació i Universitats with funds from the ERDF (SINCO2022/18146 - Plataforma HiTech-IAC3-BIO). T.A.F acknowledges support from

the São Paulo Research Foundation (FAPESP) under grant 2025/08599-6.

This material is based upon work supported by NSF's LIGO Laboratory which is a major facility fully funded by the National Science Foundation. LIGO was constructed and is operated by the California Institute of Technology and Massachusetts Institute of Technology with funding from the U.S. National Science Foundation under grant PHY-0757058. The authors also gratefully acknowledge the support of the Science and Technology Facilities Council (STFC) of the United Kingdom, the Max-Planck-Society (MPS), and the State of Niedersachsen/Germany for support of the construction of Advanced LIGO. The authors are grateful for the computational resources provided by the LIGO Laboratory and supported by National Science Foundation Grants PHY-0757058 and PHY-0823459.

APPENDIX

A. CANDIDATES

We list the loudest surviving outlier in each 1 Hz band for all targets in Tables 8–12, as the full number of surviving candidates is large; the complete catalog is available on Zenodo (Cheung 2026). For Terzan 10, all outliers were vetoed after the 4-th follow-up stage. For all other targets, candidates who survived the 4-th follow-up stage were ruled out by spectrogram inspection.

Table 8. Frequency parameters for the surviving Terzan 10 outliers from follow-up stage 3 ($T_{\text{coh}} = 60$ days).

f (Hz)	\dot{f} (Hz/s)	\ddot{f} (Hz/s ²)	\dddot{f} (Hz/s ³)
30.00487872	$-6.0846 \cdot 10^{-10}$	$1.2329 \cdot 10^{-19}$	$2.2965 \cdot 10^{-27}$
146.56147045	$-2.9891 \cdot 10^{-9}$	$5.8961 \cdot 10^{-19}$	$-2.0032 \cdot 10^{-27}$
329.71690102	$-6.5599 \cdot 10^{-9}$	$6.3227 \cdot 10^{-19}$	$-2.6605 \cdot 10^{-27}$

Table 9. Frequency parameters for the surviving NGC 104 outliers from follow-up stage 4 ($T_{\text{coh}} = 120$ days).

f (Hz)	\dot{f} (Hz/s)	\ddot{f} (Hz/s ²)	\dddot{f} (Hz/s ³)	$\ddot{\ddot{f}}$ (Hz/s ⁴)
40.06316482	$-3.1890 \cdot 10^{-10}$	$2.4479 \cdot 10^{-19}$	$-1.7670 \cdot 10^{-27}$	$-1.7552 \cdot 10^{-33}$
70.03539391	$-5.4433 \cdot 10^{-10}$	$-1.9565 \cdot 10^{-20}$	$2.1001 \cdot 10^{-27}$	$1.5305 \cdot 10^{-33}$
270.52421253	$-5.8923 \cdot 10^{-9}$	$1.2256 \cdot 10^{-18}$	$2.6355 \cdot 10^{-27}$	$-2.1168 \cdot 10^{-33}$
283.92794347	$-1.2500 \cdot 10^{-9}$	$-3.1553 \cdot 10^{-20}$	$-1.5304 \cdot 10^{-27}$	$-5.0880 \cdot 10^{-34}$
315.00274203	$-2.8860 \cdot 10^{-8}$	$1.4468 \cdot 10^{-17}$	$6.3296 \cdot 10^{-27}$	$-1.9352 \cdot 10^{-35}$
379.00551396	$-2.7534 \cdot 10^{-9}$	$1.3408 \cdot 10^{-19}$	$-5.8579 \cdot 10^{-29}$	$1.4795 \cdot 10^{-33}$
445.61972296	$-1.8802 \cdot 10^{-9}$	$5.0345 \cdot 10^{-20}$	$-9.8901 \cdot 10^{-28}$	$-9.9413 \cdot 10^{-35}$

Table 10. Frequency parameters for the surviving NGC 6397 outliers from follow-up stage 4 ($T_{\text{coh}} = 120$ days).

f (Hz)	\dot{f} (Hz/s)	\ddot{f} (Hz/s ²)	\dddot{f} (Hz/s ³)	$\ddot{\ddot{f}}$ (Hz/s ⁴)
283.94864270	$-4.9032 \cdot 10^{-9}$	$1.5520 \cdot 10^{-19}$	$3.0986 \cdot 10^{-27}$	$2.0157 \cdot 10^{-33}$
379.01949516	$-6.2017 \cdot 10^{-9}$	$2.3713 \cdot 10^{-19}$	$-3.4899 \cdot 10^{-28}$	$5.0707 \cdot 10^{-34}$
388.54366280	$-6.5297 \cdot 10^{-9}$	$8.7395 \cdot 10^{-20}$	$1.1702 \cdot 10^{-27}$	$2.6488 \cdot 10^{-34}$
426.68342796	$-7.0999 \cdot 10^{-9}$	$9.5778 \cdot 10^{-19}$	$3.0373 \cdot 10^{-27}$	$5.2953 \cdot 10^{-34}$
430.01914868	$-7.3224 \cdot 10^{-9}$	$6.7886 \cdot 10^{-19}$	$-2.6481 \cdot 10^{-27}$	$-9.8514 \cdot 10^{-34}$
436.16602540	$-7.3649 \cdot 10^{-9}$	$8.7411 \cdot 10^{-19}$	$4.9891 \cdot 10^{-28}$	$-2.1974 \cdot 10^{-33}$
449.60274465	$-7.9046 \cdot 10^{-9}$	$5.3481 \cdot 10^{-19}$	$-1.5320 \cdot 10^{-27}$	$1.5738 \cdot 10^{-33}$
469.68101671	$-3.5000 \cdot 10^{-8}$	$8.8900 \cdot 10^{-18}$	$-6.8578 \cdot 10^{-27}$	$3.2041 \cdot 10^{-34}$
472.98257180	$-4.6830 \cdot 10^{-8}$	$9.8280 \cdot 10^{-18}$	$-6.4670 \cdot 10^{-27}$	$-3.1365 \cdot 10^{-34}$
473.77676000	$-8.0640 \cdot 10^{-9}$	$1.0164 \cdot 10^{-18}$	$-3.8945 \cdot 10^{-27}$	$-9.4315 \cdot 10^{-34}$

Table 11. Frequency parameters for the surviving NGC 6544 outliers from follow-up stage 4 ($T_{\text{coh}} = 120$ days).

f (Hz)	\dot{f} (Hz/s)	\ddot{f} (Hz/s ²)	\dddot{f} (Hz/s ³)	$\ddot{\ddot{f}}$ (Hz/s ⁴)
30.00488706	$-6.0869 \cdot 10^{-10}$	$2.3406 \cdot 10^{-19}$	$2.0249 \cdot 10^{-27}$	$1.2809 \cdot 10^{-33}$
473.93176396	$-2.1467 \cdot 10^{-8}$	$7.7339 \cdot 10^{-18}$	$2.9838 \cdot 10^{-27}$	$-1.0475 \cdot 10^{-33}$

Table 12. Frequency parameters for the surviving NGC 6540 outliers from follow-up stage 4 ($T_{\text{coh}} = 120$ days).

f (Hz)	\dot{f} (Hz/s)	\ddot{f} (Hz/s ²)	\dddot{f} (Hz/s ³)	$\ddot{\ddot{f}}$ (Hz/s ⁴)
70.04033430	$-1.4219 \cdot 10^{-9}$	$3.4912 \cdot 10^{-19}$	$-1.5183 \cdot 10^{-27}$	$4.9406 \cdot 10^{-34}$
329.71744877	$-6.5881 \cdot 10^{-9}$	$2.3124 \cdot 10^{-19}$	$-6.3276 \cdot 10^{-28}$	$3.2736 \cdot 10^{-34}$
463.94293956	$-2.1718 \cdot 10^{-8}$	$3.3800 \cdot 10^{-18}$	$-1.7217 \cdot 10^{-27}$	$-1.0776 \cdot 10^{-33}$

B. SATURATED SUB-BANDS

Some frequency bands were so badly contaminated by instrumental lines that one or more jobs are saturated (≥ 1000 candidates) in the initial search. All 0.1-Hz bands with saturation in at least one \dot{f} sub-range are listed in Tables 13. We do not claim strain upper limits to signals in these sub-bands, which sum to 28.4/28.5/28.5/32.7/28.6 Hz for Terzan 10/NGC 6544/NGC 104/NGC 6397/NGC 6540 over the search range of 20–475 Hz.

REFERENCES

- Aasi, J., et al. 2015a, *Class. Quantum Grav.*, 32, 7
- . 2015b, *Classical and Quantum Gravity*, 32, 074001, doi: [10.1088/0264-9381/32/7/074001](https://doi.org/10.1088/0264-9381/32/7/074001)
- Aasi, J., Abbott, B., Abbott, R., et al. 2015c, *The Astrophysical Journal*, 813, 39, doi: [10.1088/0004-637X/813/1/39](https://doi.org/10.1088/0004-637X/813/1/39)
- Abac, A. G., Abbott, R., Abouelfettouh, I., et al. 2024, *The Astrophysical Journal Letters*, 970, L34, doi: [10.3847/2041-8213/ad5beb](https://doi.org/10.3847/2041-8213/ad5beb)
- Abac, A. G., Abouelfettouh, I., Acernese, F., et al. 2025, *Open Data from LIGO, Virgo, and KAGRA through the First Part of the Fourth Observing Run*. <https://arxiv.org/abs/2508.18079>
- Abadie, J., Abbott, B. P., Abbott, R., et al. 2010, *The Astrophysical Journal*, 722, 1504–1513, doi: [10.1088/0004-637x/722/2/1504](https://doi.org/10.1088/0004-637x/722/2/1504)
- Abbott, B., et al. 2008, *Phys. Rev. D*, 77, 022001
- . 2016, *Phys. Rev. Lett.*, 116, 131103
- Abbott, B. P., et al. 2017, *Phys. Rev. D*, 95, 082005, doi: [10.1103/PhysRevD.95.082005](https://doi.org/10.1103/PhysRevD.95.082005)
- . 2019, *The Astrophysical Journal*, 875, 122, doi: [10.3847/1538-4357/ab113b](https://doi.org/10.3847/1538-4357/ab113b)
- Abbott, R., Abbott, T. D., Acernese, F., et al. 2022, *Phys. Rev. D*, 105, 082005, doi: [10.1103/PhysRevD.105.082005](https://doi.org/10.1103/PhysRevD.105.082005)
- Abbott, R., et al. 2021a, *Phys. Rev. D*, 104, 082004, doi: [10.1103/PhysRevD.104.082004](https://doi.org/10.1103/PhysRevD.104.082004)
- . 2021b, *Astrophysical Journal*, 921, 80
- Acernese, F., et al. 2015, *Classical and Quantum Gravity*, 32, 024001, doi: [10.1088/0264-9381/32/2/024001](https://doi.org/10.1088/0264-9381/32/2/024001)
- Aharonian, F., Akhperjanian, A. G., Aye, K.-M., et al. 2005, *Science*, 307, 1938, doi: [10.1126/science.1108643](https://doi.org/10.1126/science.1108643)
- Akutsu, T., Ando, M., Arai, K., et al. 2020, *Progress of Theoretical and Experimental Physics*, 2021, 05A101, doi: [10.1093/ptep/ptaa125](https://doi.org/10.1093/ptep/ptaa125)
- Allen, B., Goetz, E., Keitel, D., et al. 2025, *SFT Data Format Version 2–3 Specification*. <https://dcc.ligo.org/LIGO-T040164/public>
- Alpar, M. A., Cheng, A. F., Ruderman, M. A., & Shaham, J. 1982, *Nature*, 300, 728, doi: [10.1038/300728a0](https://doi.org/10.1038/300728a0)
- Andersson, N. 1998, *Astrophysical Journal*, 502, 708
- Bailes, M., Bates, S. D., Bhalerao, V., et al. 2011, *Science*, 333, 1717–1720, doi: [10.1126/science.1208890](https://doi.org/10.1126/science.1208890)
- Behnke, B., Papa, M. A., & Prix, R. 2015, *Phys. Rev. D*, 91, 064007, doi: [10.1103/PhysRevD.91.064007](https://doi.org/10.1103/PhysRevD.91.064007)
- Behrens, E. A., Ransom, S. M., Madison, D. R., et al. 2020, *The Astrophysical Journal Letters*, 893, L8, doi: [10.3847/2041-8213/ab8121](https://doi.org/10.3847/2041-8213/ab8121)
- Bildsten, L. 1998, *Astrophysical Journal Letters*, 501, L89
- Bondarescu, R., Teukolsky, S. A., & Wasserman, I. 2009, *Phys. Rev. D*, 79, 104003, doi: [10.1103/PhysRevD.79.104003](https://doi.org/10.1103/PhysRevD.79.104003)
- Capote, E., Jia, W., Aritomi, N., et al. 2025, *Physical Review D*, 111, doi: [10.1103/physrevd.111.062002](https://doi.org/10.1103/physrevd.111.062002)
- Caride, S., Inta, R., Owen, B. J., & Rajbhandari, B. 2019, *Phys. Rev. D*, 100, 064013, doi: [10.1103/PhysRevD.100.064013](https://doi.org/10.1103/PhysRevD.100.064013)
- Cheung, D. 2026, *Outlier parameters from the search for continuous gravitational waves from five globular clusters in the first part of LIGO-Virgo-KAGRA forth observing run*, Zenodo, doi: [10.5281/zenodo.18426313](https://doi.org/10.5281/zenodo.18426313)
- Clark, G. W. 1975, *ApJL*, 199, L143, doi: [10.1086/181869](https://doi.org/10.1086/181869)
- Covas, P., et al. 2018, *Phys. Rev. D*, 97, 082002
- Cutler, C. 2002, *Physical Review D*, 66, 084025
- Cutler, C., & Schutz, B. F. 2005, *Phys. Rev. D*, 72, 063006, doi: [10.1103/PhysRevD.72.063006](https://doi.org/10.1103/PhysRevD.72.063006)
- Dartez, L., et al. 2025, *Characterization of Systematic Error in Advanced LIGO Calibration in the Fourth Observing Run*. <https://dcc.ligo.org/P2400219>
- Davis, D., Neunzert, A., Goetz, E., et al. 2024, *Self-gating of O4a h(t) for use in continuous-wave searches*. <https://dcc.ligo.org/T2400003>
- Dunn, L., Melatos, A., Clearwater, P., et al. 2025, *Phys. Rev. D*, 111, 083012, doi: [10.1103/PhysRevD.111.083012](https://doi.org/10.1103/PhysRevD.111.083012)
- Friedman, J., & Morsink, S. 1998, *Astrophys. J.*, 502, 714
- Ganapathy, D., Jia, W., Nakano, M., et al. 2023, *Phys. Rev. X*, 13, 041021, doi: [10.1103/PhysRevX.13.041021](https://doi.org/10.1103/PhysRevX.13.041021)
- Gittins, F., & Andersson, N. 2023, *Monthly Notices of the Royal Astronomical Society*, 521, 3043, doi: [10.1093/mnras/stad672](https://doi.org/10.1093/mnras/stad672)
- Glampedakis, K., & Gualtieri, L. 2018, *Gravitational waves from single neutron stars: an advanced detector era survey*, Vol. 457, 673–736
- Goetz, E., & Riles, K. 2025, *Segments used for creating standard SFTs in O4 data*. <https://dcc.ligo.org/T2400058-v2/public>
- Goetz, E., Kalmus, P., Erickson, S., et al. 2009, *Classical and Quantum Gravity*, 26, 245011, doi: [10.1088/0264-9381/26/24/245011](https://doi.org/10.1088/0264-9381/26/24/245011)
- Goetz, E., et al. 2024, *O4a lines and combs in found in self-gated C00 cleaned data*. <https://dcc.ligo.org/T2400204>
- Harris, W. E. 1996, *AJ*, 112, 1487, doi: [10.1086/118116](https://doi.org/10.1086/118116)
- Haskell, B., Andersson, N., Jones, D. I., & Samuelsson, L. 2007, *Physical Review Letters*, 99, doi: [10.1103/physrevlett.99.231101](https://doi.org/10.1103/physrevlett.99.231101)
- Idrisy, A., Owen, B. J., & Jones, D. I. 2015, *Phys. Rev. D*, 91, 024001, doi: [10.1103/PhysRevD.91.024001](https://doi.org/10.1103/PhysRevD.91.024001)

- Jaranowski, P., Krolak, A., & Schutz, B. 1998a, *Phys. Rev. D*, 58, 063001
- Jaranowski, P., Królak, A., & Schutz, B. F. 1998b, *Physical Review D*, 58, 063001, doi: [10.1103/PhysRevD.58.063001](https://doi.org/10.1103/PhysRevD.58.063001)
- Jia, W., et al. 2024, *Science*, 385, 1318, doi: [10.1126/science.ado8069](https://doi.org/10.1126/science.ado8069)
- Johnson-McDaniel, N. K., & Owen, B. J. 2013, *Phys. Rev. D*, 88, 044004, doi: [10.1103/PhysRevD.88.044004](https://doi.org/10.1103/PhysRevD.88.044004)
- Karki, S., Tuyenbayev, D., Kandhasamy, S., et al. 2016, *Review of Scientific Instruments*, 87, doi: [10.1063/1.4967303](https://doi.org/10.1063/1.4967303)
- Katz, J. I. 1975, *Nature*, 253, 698, doi: [10.1038/253698a0](https://doi.org/10.1038/253698a0)
- Kojima, Y. 1998, *Mon. Not. Roy. Astron. Soc.*, 293, 49
- Lasky, P. 2015, *Pub. Astron. Soc. Aust.*, 32, e034
- Lasky, P. D., & Melatos, A. 2013, *Physical Review D*, 88, 103005, doi: [10.1103/PhysRevD.88.103005](https://doi.org/10.1103/PhysRevD.88.103005)
- Lorimer, D. R. 2008, *Living Rev. Rel.*, 11, 8, doi: [10.12942/lrr-2008-8](https://doi.org/10.12942/lrr-2008-8)
- Nițu, I. C., Keith, M. J., Stappers, B. W., Lyne, A. G., & Mickaliger, M. B. 2022, *Monthly Notices of the Royal Astronomical Society*, 512, 2446–2459, doi: [10.1093/mnras/stac593](https://doi.org/10.1093/mnras/stac593)
- Owen, B., et al. 1998, *Phys. Rev. D*, 58, 084020
- Owen, B. J. 2010, *Phys. Rev. D*, 82, 104002, doi: [10.1103/PhysRevD.82.104002](https://doi.org/10.1103/PhysRevD.82.104002)
- Palomba, C. 2005, *Monthly Notices of the Royal Astronomical Society*, 359, 1150, doi: [10.1111/j.1365-2966.2005.08975.x](https://doi.org/10.1111/j.1365-2966.2005.08975.x)
- Piccinni, O. J. 2022, *Galaxies*, 10, doi: [10.3390/galaxies10030072](https://doi.org/10.3390/galaxies10030072)
- Pooley, D., Lewin, W. H. G., Anderson, S. F., et al. 2003, *ApJL*, 591, L131, doi: [10.1086/377074](https://doi.org/10.1086/377074)
- Riles, K. 2023, *Living Rev. Rel.*, 26, 3, doi: [10.1007/s41114-023-00044-3](https://doi.org/10.1007/s41114-023-00044-3)
- Soni, S., Berger, B. K., Davis, D., et al. 2025, *Classical and Quantum Gravity*, 42, 085016, doi: [10.1088/1361-6382/adc4b6](https://doi.org/10.1088/1361-6382/adc4b6)
- Spiewak, R., Bailes, M., Barr, E. D., et al. 2018, *MNRAS*, 475, 469, doi: [10.1093/mnras/stx3157](https://doi.org/10.1093/mnras/stx3157)
- Tenorio, R., Keitel, D., & Sintes, A. M. 2021, *Universe*, 7, doi: [10.3390/universe7120474](https://doi.org/10.3390/universe7120474)
- Ushomirsky, G., Cutler, C., & Bildsten, L. 2000, *Monthly Notices of the Royal Astronomical Society*, 319, 902, doi: [10.1046/j.1365-8711.2000.03938.x](https://doi.org/10.1046/j.1365-8711.2000.03938.x)
- Verbunt, F., & Freire, P. C. C. 2014, *Astron. Astrophys.*, 561, A11, doi: [10.1051/0004-6361/201321177](https://doi.org/10.1051/0004-6361/201321177)
- Viets, A. D., Wade, M., Urban, A. L., et al. 2018, *Classical and Quantum Gravity*, 35, 095015, doi: [10.1088/1361-6382/aab658](https://doi.org/10.1088/1361-6382/aab658)
- Wade, M., Betzwieser, J., Bhattacharjee, D., et al. 2025, *Classical and Quantum Gravity*, 42, 215016, doi: [10.1088/1361-6382/ae1095](https://doi.org/10.1088/1361-6382/ae1095)
- Wang, J., & Riles, K. 2024, *Phys. Rev. D*, 110, 042006, doi: [10.1103/PhysRevD.110.042006](https://doi.org/10.1103/PhysRevD.110.042006)
- Wang, Z., Chakrabarty, D., & Kaplan, D. L. 2006, *Nature*, 440, 772–775, doi: [10.1038/nature04669](https://doi.org/10.1038/nature04669)
- Wette, K. 2014, *Phys. Rev. D*, 90, 122010
- . 2015, *Phys. Rev. D*, 92, 082003
- . 2023, *Astropart. Phys.*, 153, 102880, doi: [10.1016/j.astropartphys.2023.102880](https://doi.org/10.1016/j.astropartphys.2023.102880)
- Wette, K., & Prix, R. 2013, *Phys. Rev. D*, 88, 123005
- Wette, K., et al. 2008, *Class. Quant. Grav.*, 25, 235011
- . 2018, *Phys. Rev. D*, 97, 123016
- Wolszczan, A., & Frail, D. A. 1992, *Nature*, 355, 145, doi: [10.1038/355145a0](https://doi.org/10.1038/355145a0)